Modeling the Flow Behavior, Recrystallization, and Crystallographic Texture in Hot-Deformed Fe-30 Wt Pct Ni Austenite

M.F. ABBOD, C.M. SELLARS, P. CIZEK, D.A. LINKENS, and M. MAHFOUF

The present work describes a hybrid modeling approach developed for predicting the flow behavior, recrystallization characteristics, and crystallographic texture evolution in a Fe-30 wt pct Ni austenitic model alloy subjected to hot plane strain compression. A series of compression tests were performed at temperatures between 850 °C and 1050 °C and strain rates between 0.1 and 10 s^{-1}. The evolution of grain structure, crystallographic texture, and dislocation substructure was characterized in detail for a deformation temperature of 950 °C and strain rates of 0.1 and 10 s^{-1}, using electron backscatter diffraction and transmission electron microscopy. The hybrid modeling method utilizes a combination of empirical, physically-based, and neuro-fuzzy models. The flow stress is described as a function of the applied variables of strain rate and temperature using an empirical model. The recrystallization behavior is predicted from the measured microstructural state variables of internal dislocation density, subgrain size, and misorientation between subgrains using a physically-based model. The texture evolution is modeled using artificial neural networks.

DOI: 10.1007/s11661-007-9292-5

I. INTRODUCTION

IT is well known that the microstructure of materials such as steel plays a vital role in dictating the deformation behavior during thermomechanical processing. The microstructure of the parent austenite also determines the final transformed microstructure, and hence the final properties. Consequently, the development of physically-based models of microstructural evolution during thermomechanical processing of metallic materials requires knowledge of the internal state variables, such as grain structure, crystallographic texture, and dislocation substructure, over a range of processing conditions. A Fe-30 wt pct Ni-based alloy has recently been shown to act as a good model material for investigation of hot deformation of austenite in conventional carbon-manganese steels.[1] This alloy has a stable austenitic structure down to room temperature, allowing the high-temperature deformation structure to be readily characterized following a rapid cool after deformation.[2] This alloy is also believed to have comparable stacking fault energy to that of carbon steels, thus implying that the deformation response should be comparable.[3]

When developing a model to predict material behavior, the ultimate aim of modeling is to provide the tools that can be extended to all conditions and for any material. At the current status, physically-based modeling is difficult to apply to such extended conditions and materials. Extending the range of application requires carrying out a considerable amount of experimental research, which is a very time-consuming process. Therefore, it is desirable to develop a modeling tool to be used for prediction under extended deformation conditions and for different types of material. The combination of physical knowledge and black-box modeling, termed hybrid modeling, is an attractive way for further development of modeling. It has been shown[4,5] that the hybrid models provide an efficient tool to simulate plastic deformation behavior and microstructure evolution during thermomechanical processing of metals, being based on more physical knowledge than either empirical models or neural network models alone.

The aim of the present work is to develop a hybrid model capable of predicting the flow behavior as well as the recrystallization characteristics and crystallographic texture evolution in an Fe-30 wt pct Ni austenitic model alloy deformed in hot plane strain compression. The flow curves will be described as a function of the applied variables of strain rate and deformation temperature. The recrystallization behavior will be predicted from the measured microstructural state variables of internal dislocation density, subgrain size, and misorientation between subgrains. The evolution of both the deformation and recrystallization texture will be modeled using a data driven approach, namely, artificial neural networks (ANNs).

M.F. ABBOD, Lecturer, is with the School of Engineering and Design, Brunel University, Uxbridge UB8 3PH, United Kingdom. Contact e-mail: maysam.abbod@brunel.ac.uk C.M. SELLARS, Emeritus Professor, Department of Engineering Materials, D.A. LINKENS, Emeritus Professor, and M. MAHFOUF, Professor, are with the Department of Automatic Control and System Engineering, The University of Sheffield, Sheffield S1 3JD, United Kingdom. P. CIZEK, Research Academic, is with the Centre for Material and Fibre Innovation, Deakin University, Geelong, Victoria 3217, Australia.

Manuscript submitted April 24, 2007.
Article published online August 29, 2007.

II. EXPERIMENTAL PROCEDURE

The material used is Fe-30 wt pct Ni-based austenitic model alloy with a chemical composition of 0.092 wt pct C, 0.19 pct Si, 1.67 pct Mn, 0.009 pct P, 0.003 pct S, 30.3 pct Ni, 1.51 pct Mo, and the balance Fe. Specimens with dimensions of $60 \times 30 \times 10$ mm were subjected to hot plane strain compression (PSC) testing using a computer-controlled thermomechanical compression machine.[6] The specimens were preheated at 1250 °C for 15 minutes, air cooled, and deformed at temperatures of 850 °C, 950 °C, and 1050 °C and strain rates of 0.1, 1, and 10 s^{-1} to a true strain level of approximately 0.7. In addition, for the deformation temperature of 950 °C and strain rates of 0.1 and 10 s^{-1}, the deformation was interrupted at true strain levels of approximately 0.2, 0.4, and 0.6 in order to study the microstructure evolution during straining. The mean recrystallized grain size obtained after preheating was about 120 μm. After testing, the PSC specimens were quenched in water within about 1 second. Investigation of the grain structure, crystallographic texture, and dislocation substructure was undertaken in the central areas of PSC specimens on sections containing the extension and normal sample directions, using quantitative light microscopy, electron backscatter diffraction (EBSD), and transmission electron microscopy (TEM) techniques. The EBSD study was performed using an FEI Sirion field-emission gun scanning electron microscope, equipped with the HKL Technology EBSD attachment, operated at 15 kV. The corresponding data acquisition and processing were carried out using the HKL Channel 5 software. The TEM examination of thin foils was performed using Philips EM420 microscope operated at 120 kV (Philips is a trademark of Philips Electronic Instruments Corp., Mahwah, NJ, USA).

The crystallographic texture was measured for the specimens deformed at a temperature of 950 °C at strain rates of 0.1 and 10 s^{-1} using the EBSD technique.[7] The texture was represented by a three-dimensional orientation distribution function (ODF) in Euler space.[7,8] The experimental ODFs were calculated in the Channel 5 software *via* superimposing Gaussian spreads of half-width of 5 deg on the measured individual orientations, using the angular notation suggested by Bunge.[8] The deformation and recrystallization textures were determined separately as a function of strain.[6]

III. FLOW BEHAVIOR MODELING

The results of the PSC tests were analyzed using standard procedures[9] to obtain equivalent true stress–equivalent true strain curves shown in Figure 1. The instantaneous temperatures during deformation were calculated using a finite difference package based on the dimensions of the specimens, the deformation conditions, and the heat transfer to the tools and environment.[10] The calculations assumed a specific heat capacity of 456 J kg^{-1} K^{-1} and material density of 7700 kg m^{-3}. The temperature rise during deformation is shown in Figure 2 for the different deformation conditions.

The curves in Figures 1 and 2 were used to develop the model for the stress-strain behavior based on the initial flow stress (σ_0), the stresses at a strain of 0.1 ($\sigma_{0.1}$), the steady-state stress expected for work hardening and dynamic recovery only ($\sigma_{ss(e)}$), and the experimental steady-state stress (σ_{ss}). These stresses were read directly from the curves and were plotted against the logarithm of the Zener–Hollomon parameter

$$Z = \dot{\varepsilon} \exp\left(\frac{Q}{RT}\right) \qquad [1]$$

where

R = gas constant (R = 8.31 J/mol K),
T = temperature is Kelvin, and
Q = activation energy (Q = 480 kJ/mol)[6]

The temperature is the actual value for the strain of interest, which gives the instantaneous values of Z shown in Figure 3. Over the entire range of Z, the curves

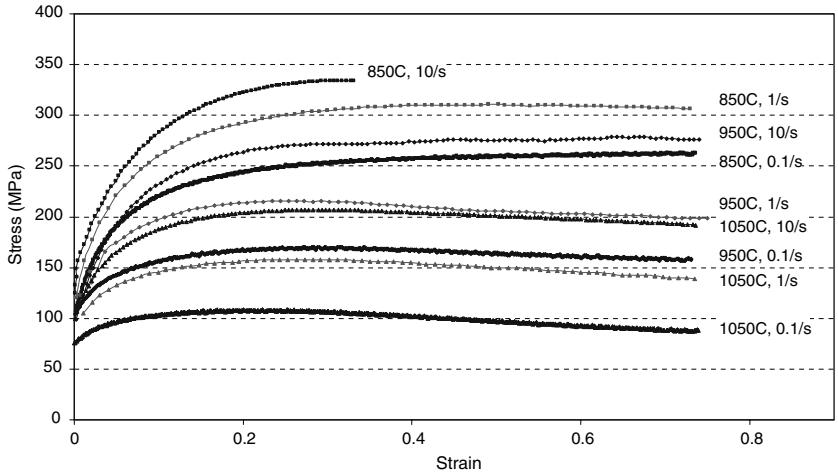

Fig. 1—Experimental equivalent stress–equivalent strain curves for different deformation conditions.

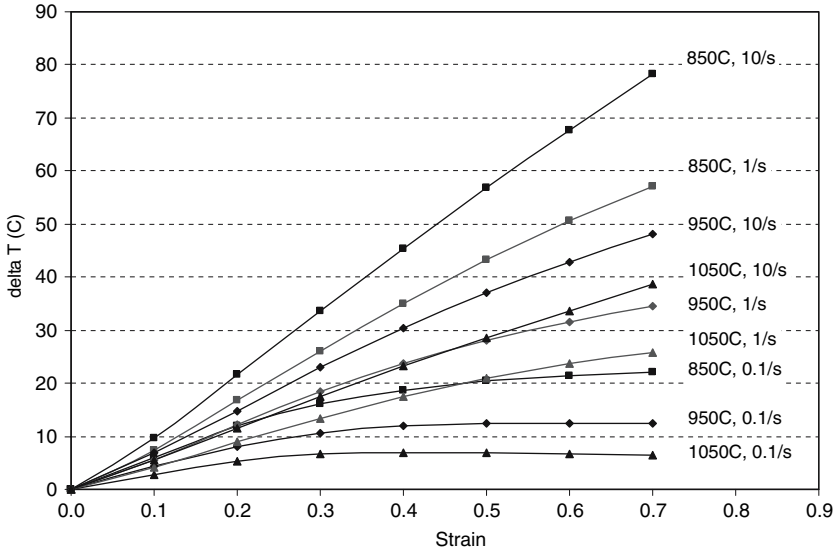

Fig. 2—Calculated temperature rise due to deformational work done during PSC tests.

in Figure 3 were fitted by the following general equation:

$$\sigma = \frac{\sinh^{-1}(Z/A)^{(1/n)}}{\alpha} \quad [2]$$

where n, A, and α are constants obtained from the optimized curves, to give the values summarized by the following equations:

$$\sigma_0 = \frac{\sinh^{-1}(Z/1.54E18)^{(1/10.63)}}{0.0127} \quad [3]$$

$$\sigma_{0.1} = \frac{\sinh^{-1}(Z/1.0E18)^{(1/7.91)}}{0.0075} \quad [4]$$

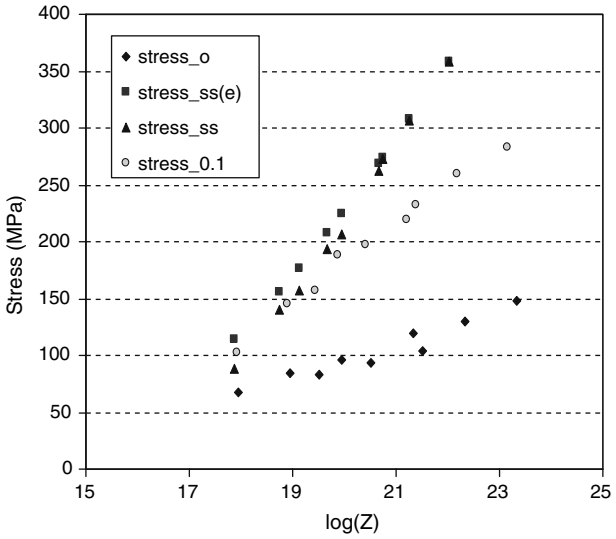

Fig. 3—Measured stresses at different strains plotted against the logarithm of the instantanenous value of the Zener–Hollomon parameter.

$$\sigma_{ss(e)} = \frac{\sinh^{-1}(Z/2.27E18)^{(1/5.25)}}{0.0065} \quad [5]$$

$$\sigma_{ss} = \frac{\sinh^{-1}(Z/0.87E18)^{(1/3.39)}}{0.0097} \quad [6]$$

It was assumed that these equations are mechanical equations of state, so that the stress-strain curves expected for isothermal deformation (*i.e.*, constant Z) conditions could be calculated and fitted to the equations:

$$\sigma' = \sigma_0 + (\sigma_{ss(e)} - \sigma_0)\left[1 - \exp\left(\frac{-\varepsilon}{\varepsilon_r}\right)\right]^{1/2} \quad [7]$$

which applies for all strains when $\sigma_{(ss)e} = \sigma_{ss}$, but only for $\varepsilon \le 0.7\ \varepsilon_p$ when $\sigma_{ss} < \sigma_{(ss)e}$. In the latter case,

$$\sigma = \sigma' - 1.0(\sigma_{ss(e)} - \sigma_{ss}) \left\{1 - \exp\left[-0.56\left(\frac{\varepsilon - 0.7\varepsilon_p}{\varepsilon_{ss}(e) - 0.7\varepsilon_p}\right)^{0.632}\right]\right\} \quad (\varepsilon \ge 0.7\varepsilon_p) \quad [8]$$

In Eq. [7], $\varepsilon_r = \varepsilon_{ss(e)}/2.3$,[11] where $\varepsilon_{ss(e)}$ is defined as the strain at which $(\sigma - \sigma_0) = 0.95\ (\sigma_{ss(e)} - \sigma_0)$ under isothermal conditions. In Eq. [8], ε_p is the strain at the peak stress when $\sigma_{ss} < \sigma_{(ss)e}$ under isothermal conditions. From optimized fits to these equations,

$$\varepsilon_{ss(e)} = 11.8 \times 10^{-3}\, Z^{0.075} \quad [9]$$

and

$$\varepsilon_p = 0.982 \times 10^{-5}\, Z^{0.23} \quad (\varepsilon_{ss(e)} \ge 0.7\varepsilon_p) \quad [10]$$

The stress-strain curves computed for isothermal conditions are shown in Figure 4. It should be noted that the stress scale in this figure has been changed because of

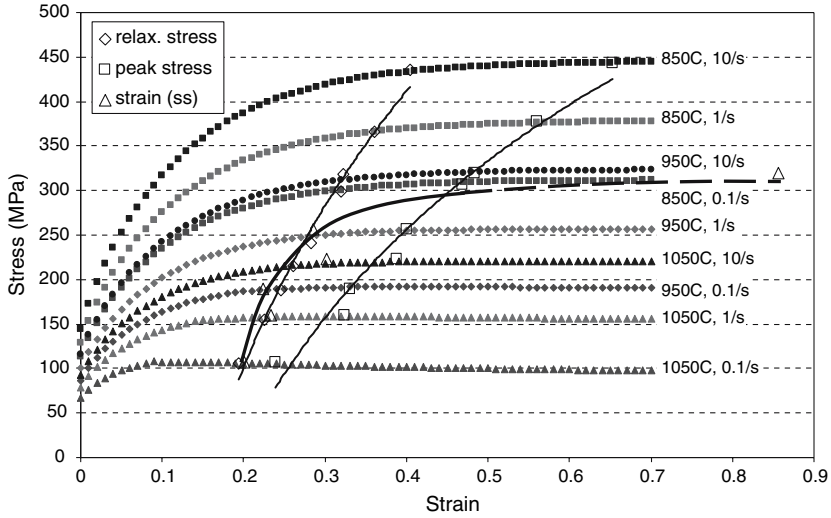

Fig. 4—Stress-strain curves for isothermal conditions.

the major effect of the temperature rise on the experimental curves. It is noteworthy that the optimized values of $\varepsilon_{ss(e)}$ and ε_p crossover as the value of Z increases. It is considered that when the critical strain for the onset of dynamic recrystallization ε_c ($\varepsilon_c = 0.7\varepsilon_p$) becomes larger than the strain due to the onset of the steady state by work hardening and dynamic recovery only ($\varepsilon_{ss(e)}$), dynamic recrystallization will not be nucleated.

Using these modeled values for the constants in Eqs. [7] and [8], together with the computed temperature rise under the experimental conditions, leads to the curves in Figure 5. It can be seen that these are in good agreement with the experimental points for all the experimental conditions.

IV. RECRYSTALLIZATION MODELING

The physically-based models used in the present article have been described in detail elsewhere.[12,13] In order to have the inputs for the deformed microstructures, the mean values of subgrain size, δ, and the misorientation across subgrain boundaries, θ, were determined from the EBSD measurements of specimens deformed at 950 °C and strain rates of 0.1 and 10 s^{-1} to different strains and water quenched. Measurements were made only in the unrecrystallized regions of the specimens, and the results are shown in Figures 6(a) and (b). The austenite substructure was found to be rather heterogeneous and subgrains were frequently arranged in elongated "microbands" in agreement with the previously observed characteristics of hot-deformed austenite.[14–17] The internal dislocation structure present within the subgrain interiors was observed by transmission electron microscopy and was relatively high, but heterogeneous densities were found for both strain rates at 950 °C. The mean dislocation density values were not measured directly, but were estimated from the flow stresses (Figure 1). From the results of changing strain rate tests,[18] it is expected that the

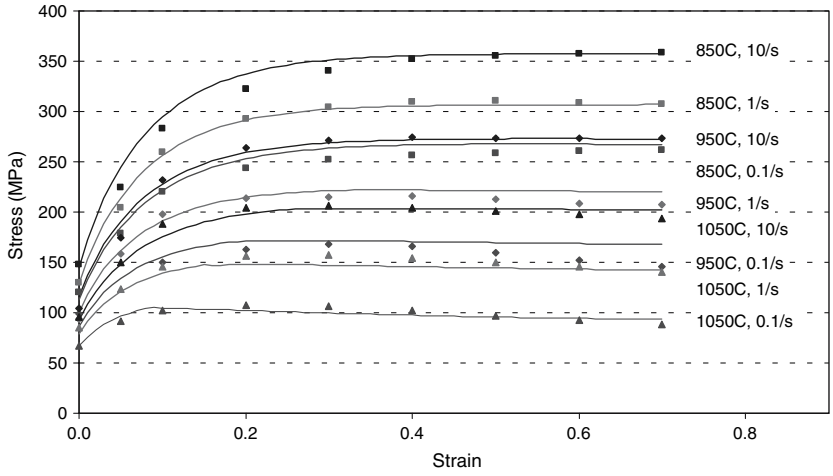

Fig. 5—Experimental (points) and modeled (solid lines) stress-strain curves for different deformation conditions.

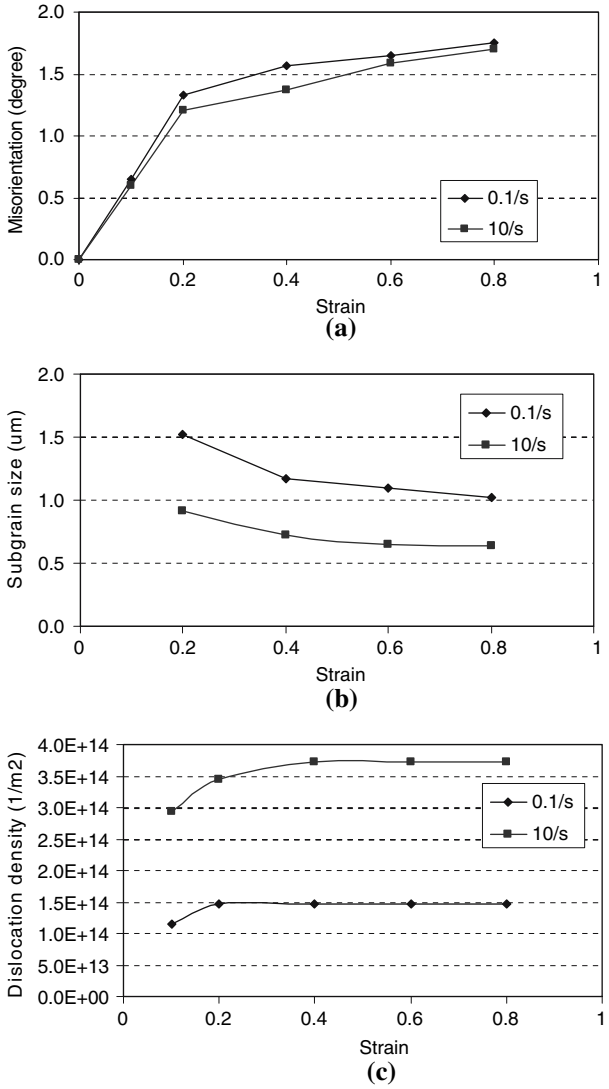

Fig. 6—Internal states of specimens deformed at 950 °C: (*a*) measured subgrain size, (*b*) measured subgrain boundary misorientation, and (*c*) estimated internal dislocation density.

internal dislocation density, rather than the subgrain structure, determines the flow stress as

$$\sigma = \sigma_f + \alpha \mathrm{M} G \mathbf{b} \rho i^{1/2} \qquad [11]$$

where σ_f is the friction stress, assumed (arbitrarily) to account for half the flow stress for the present calculations, and M is the Taylor factor (3.1), and G is the shear modulus (81×10^9). The resulting values of ρ_i are shown in Figure 6(c).

Only limited experimental data on recrystallization are available for the specimens water quenched after a delay of about 1 second following deformation at 950 °C and strain rates of 0.1 and 10 s^{-1} to different strains.[6,15] Observations made at strains giving approximately the same fractions recrystallized at the two strain rates are shown in Figure 7. There are too few data to be able to model the overall recrystallization behavior, but the procedure developed for modeling static recrystallization of aluminum alloys[19,20] can be applied to analyze the effects of the different deformation conditions at 950 °C on the present Fe-30 wt pct Ni alloy. From physical metallurgy, the time for 50 pct static recrystallization, t_{50}, is determined by the density of nucleation sites per unit volume, N_v, the stored energy per unit volume, P_D, and the grain boundary mobility, M_{gb}, as[21]

$$t_{50} = C N_v^{-1/3} P_D^{-1} M_{gb}^{-1} \qquad [12]$$

where C is a numerical constant.

The experimental observations (Figure 7) show clearly that grain boundaries are the preferred nucleation sites, and for the present initial grain size, d_0, and range of subgrain sizes, δ, nucleation at grain boundary surfaces is dominant, so the equation for nucleation density[21] can be simplified to

$$N_v = p_3 \lambda_3 S_v / \delta^2 \qquad [13]$$

For deformation in plane strain compression, the value of S_v increases with the increase in equivalent strain, ε, as[21]

$$S_v = d_0^{-1}[0.429 \exp(-\sqrt{3}\varepsilon/2) + 0.571 + \exp(\sqrt{3}\varepsilon/2)] \qquad [14]$$

The stored energy depends on the dislocation density inside subgrains, ρ_i, the subgrain size, δ, and boundary misorientation, θ, as[21]

$$P_{\mathrm{D}} = \frac{G\mathbf{b}^2}{10}\left[\rho_{\mathrm{i}}\left(1 - \ln\left(10\mathbf{b}\rho_i^{1/2}\right)\right) + \frac{2\theta}{\mathbf{b}\delta}\left(1 + \ln\left(\frac{\theta_{\mathrm{c}}}{\theta}\right)\right)\right] \qquad [15]$$

where G is the shear modulus (81×10^9), $\mathbf{b}$ is the Burgers vector (0.258×10^{-9} m), and θ_{c} is the critical angle for distinguishing a grain boundary and a subgrain boundary, and is assumed to be 15 deg.

The grain boundary mobility is not known, but it is assumed that its temperature dependence is given by

$$M_{gb} = M_{gb0} \exp(-Q/RT) \qquad [16]$$

where M_{gbo} is a constant; and Q is the activation energy for boundary migration, which, by analogy with observations on the highly alloyed stainless steels, is assumed to be similar to the value for hot deformation, *i.e.*, 480 kJ/mol.

Because of the unknown constants and the various assumptions made previously, the calculated values of t_{50} have been normalized to t_{50}* by dividing them by the value calculated for recrystallization at 950 °C after deformation at 950 °C and a strain rate of 0.1 s^{-1} to a strain of 0.1. The resulting dependence of t_{50}* on strain is shown in Figure 8, in which the broken curves show the results, if there were no dynamic recrystallization and annealing were carried out at 950 °C. At strain rates of both 0.1 s^{-1} and 10 s^{-1}, the values of t_{50}* decrease gradually with strain, by factors of 2.9 and 3.4, respectively, because of the effects of strain on S_v, δ, θ, and ρ_i. However, by extrapolation in Figure 2, deformational heating produces a temperature rise of about 12 °C and 52 °C by a strain of 0.8 at the two strain rates.

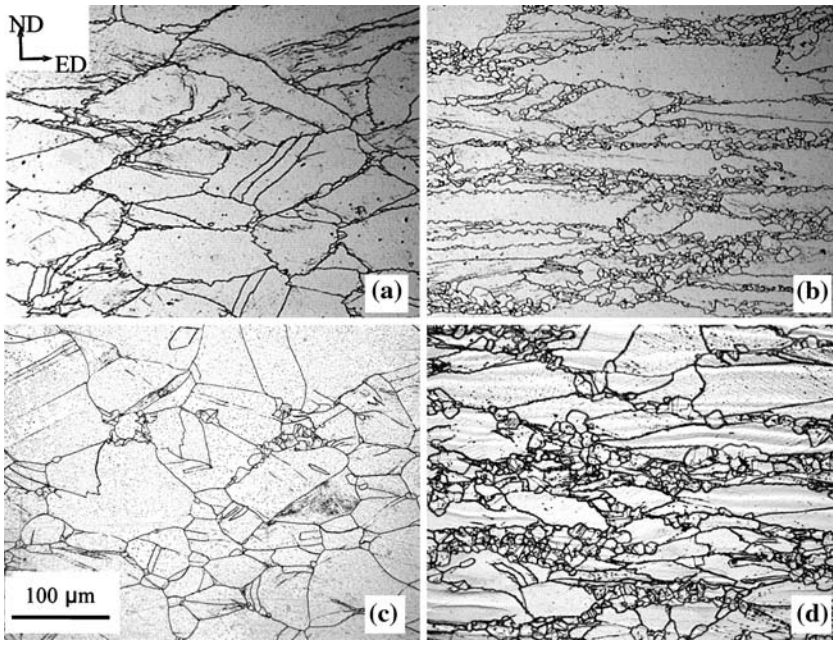

Fig. 7—Optical micrographs showing the longitudinal section of PSC test specimens deformed at 950 °C and a strain rate of 0.1 s^{-1} to strains of (*a*) 0.4 and (*b*) 0.8 and at a strain rate of 10 s^{-1} to strains of (*c*) 0.2 and (*d*) 0.6.

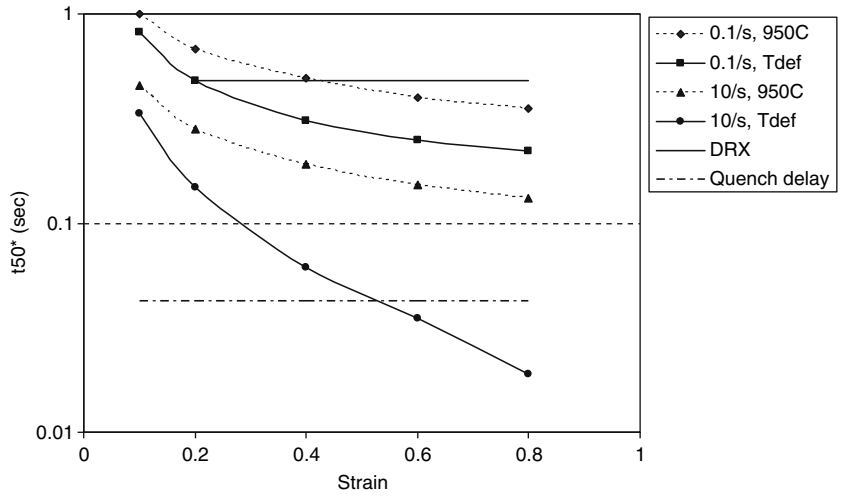

Fig. 8—Normalized time for 50 pct recrystallization for different deformation conditions.

In the short time before quenching, after which recrystallization was observed, it can be assumed that annealing takes place at the final deformation temperature. The values of t_{50}* given by the solid curves now show major differences in the effects of strain at the two strain rates. At a strain rate of 0.1 s^{-1}, the factor has increased slightly to 3.4, but at 10 s^{-1}, it has increased to 18.

A quench delay time is sketched in by the chain line to cross the curve for 10 s^{-1} at approximately the strain when 50 pct recrystallization was observed experimentally in the quenched specimens.[6,15] Because the delay is about 1 second, this gives an absolute time scale for estimating t_{50}. At a strain rate of 0.1 s^{-1}, 1.7 pct recrystallization is observed at a strain of 0.2. If this is the start of dynamic recrystallization, it would be consistent with the curve for ε_p crossing the stress-strain curve for 950 °C and 0.1 s^{-1} at a strain of 0.26 (Figure 4). By analogy with data on other steels in the austenitic condition,[22] the time for 50 pct recrystallization is expected to become independent of strain when dynamic recrystallization has taken place. This is shown by the horizontal line labeled DRX in Figure 8.

V. CRYSTALLOGRAPHIC TEXTURE MODELING

The starting texture of the material after heat treatment, as measured by EBSD, was rather weak, being characterized by the maximum of 1.7 times random

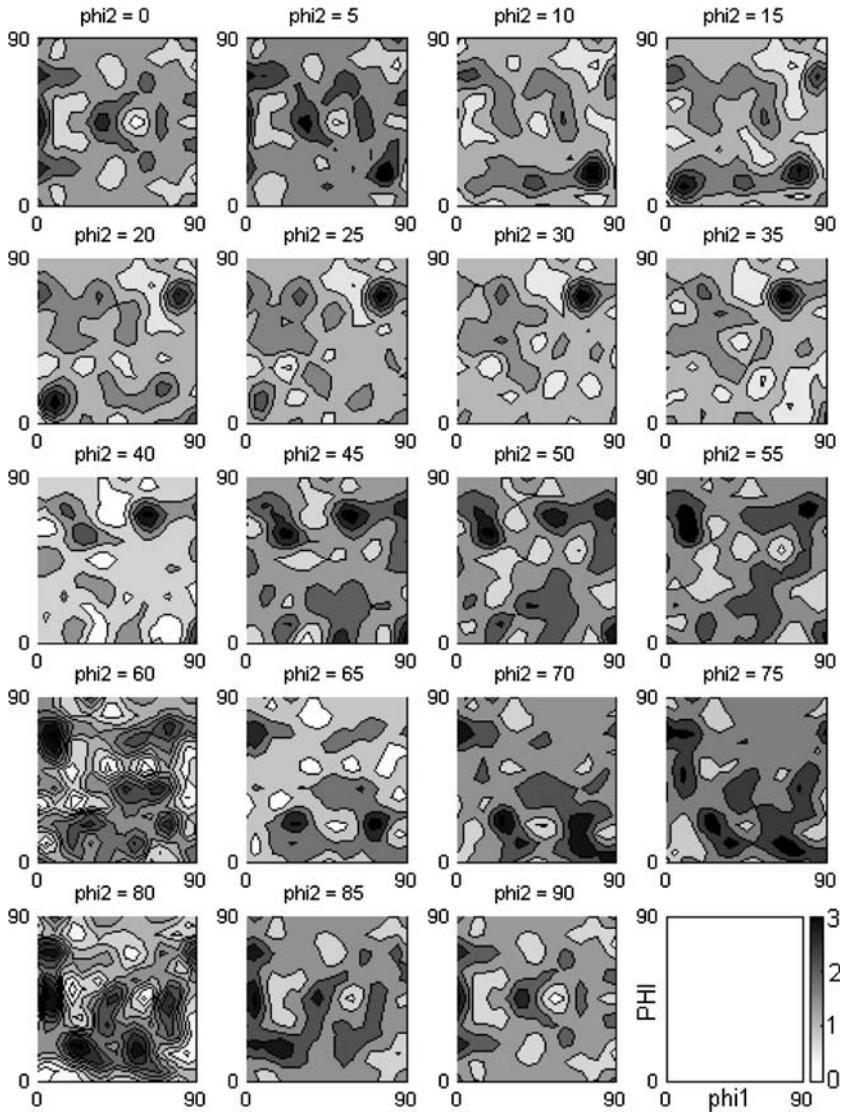

Fig. 9—Initial crystallographic texture.

(Figure 9). For both the strain rates studied, the deformation texture was predominantly composed of orientations clustered around the copper $\{112\}<111>$, S $\{123\}<634>$, brass $\{011\}<211>$, and Goss $\{011\}<100>$ texture components.[6,15,17] There was also some limited presence of the cube $\{001\}<100>$ components in the orientation distributions, in particular at a strain rate of 10 s^{-1}. The overall strength of the deformation texture gradually increased with strain and the relative intensities of the preceding main texture components varied as a function of strain. The recrystallization textures were rather weak and consisted mainly of cube and brass components. An example of the measured ODFs after a strain of 0.6 is shown in Figure 10(a) for deformation texture and in Figure 10(b) for recrystallization texture.

In order to model the texture evolution, a systems modeling approach has been introduced to replicate the Taylor equation in the modeling framework for texture prediction. The approach is based on a data-driven systems modeling technique, which utilizes experimental data for individual orientations with their deformation conditions (temperature and strain) and models the rotations of these orientations using neural networks,[23] as schematically illustrated in Figure 11. The neural network model has been trained using experimental data points represented by the measured deformation or recrystallization texture orientations (Euler angle triplets φ_1, Φ, and φ_2) related to a particular strain and temperature and the corresponding starting texture orientations. With a single hidden layer of 50 neurons in a feed-forward, back-propagation network, the system was trained for 50 epochs. Two networks have been trained, the first for the deformation texture and the second for the recrystallization texture as a function of strain. Figure 12 shows the modeled deformation and recrystallization textures after a strain of 0.6, for direct comparison with Figure 10. It can be seen that the model is able to capture all the important features of the experimentally obtained ODFs.

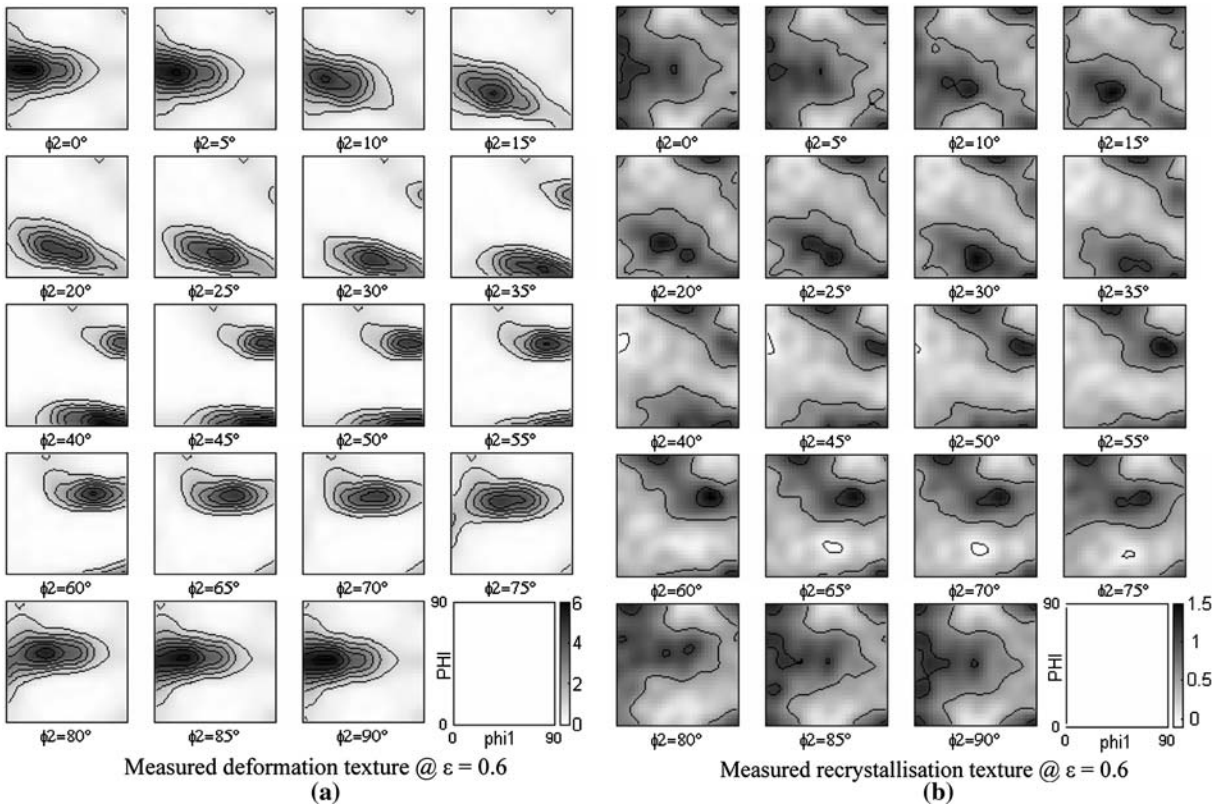

Fig. 10—The evolution of deformation and recrystallization texture determined using the EBSD technique and expressed by the ODF in Bunge notation.[8] Deformation conditions: strain rate = 10/s, and temperature = 950 °C.

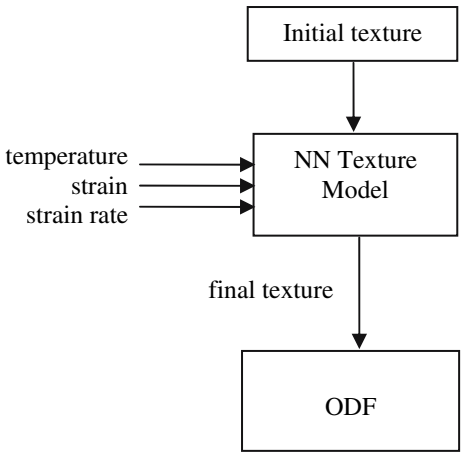

Fig. 11—Systems approach texture model.

VI. DISCUSSION

As shown in Section III, in defining the values of strain to steady state ($\varepsilon_{ss(e)}$), when dynamic recovery is controlling, and of strain to the peak stress (ε_p), when dynamic recrystallization takes place, it is important to derive the stress-strain curves for isothermal conditions to eliminate the effects of temperature rise, which differ for the different strain rates (Figure 2). When the values of these critical strains are superimposed on the stress-strain curves (Figure 4), it can be seen that the critical strains cross over at a value of $Z = 2.5 \times 10^{22}$ s^{-1}. The simple interpretation of the crossover is that at higher values of Z, there will be no dynamic recrystallization, but at lower values of Z, dynamic recrystallization will reduce the steady-state stress by increasingly significant amounts as Z decreases. This is consistent with the changing shape of the stress-strain curves in Figures 1 and 4 and, as discussed later, with the microstructural observations of recrystallization.

The experimental work is based on PSC tests in which the strain and strain rate distributions are characteristically heterogeneous.[24] This means that the local strain rate and accumulated strain on the active slip line fields differ from the nominal strain values calculated from the changes in specimen geometry. This has the consequence that equivalent stress (nominal)–equivalent strain curves, as shown in Figures 1, 4, and 5, have a dependence on the initial specimen geometry as well as on the material properties. From finite element modeling,[24] a correction procedure has been developed to relate the flow stress to the slip line field strain rate and strain.[25] This modifies the stress strain curves and eliminates the geometry effect, so that the corrected curves give constitutive equations that reflect the true material behavior and can be applied accurately in modeling any type of hot deformation process. Equations [3] through [6], and [9] and [10], have been corrected using the preceding procedure, and the new

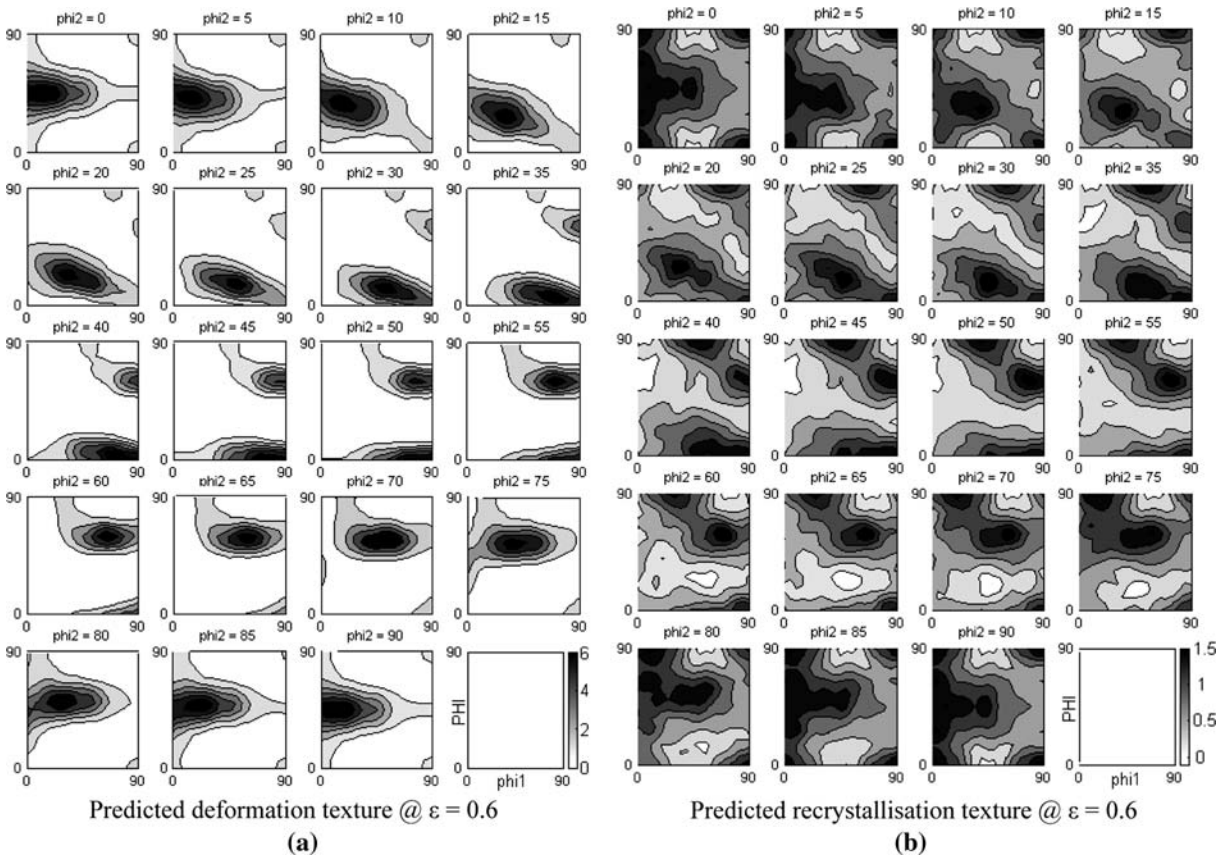

Fig. 12—Prediction *via* ANN of the evolution of deformation and recrystallization texture expressed by the ODF in Bunge notation.[8] Deformation conditions: strain rate = 10/s, and temperature = 950 °C.

parameters (SLF correction) are compared with the original ones (no correction) in Table. I.

From optimized fits to these equations,

$$\varepsilon_{ss(e)(\mathrm{SLF})} = 12.1 \times 10^{-3}\ Z^{0.074} \qquad [17]$$

and

$$\varepsilon_{p(\mathrm{SLF})} = 0.992 \times 10^{-5} Z^{0.23} \quad (\varepsilon_{ss(e)} \geq 0.7\varepsilon_p) \qquad [18]$$

The analysis of the normalized time for 50 pct recrystallization in Figure 8 is particularly relevant for interpreting the limited experimental data on recrystallization observed in specimens quenched after about 1 second following the end of deformation. For a strain rate of 0.1 s^{-1}, the t_{50} line for recrystallization after dynamic recrystallization is at a time more than an order of magnitude longer than the quench delay time (*i.e.*, about 11 seconds). If the Avrami coefficient is 2, this means that negligible static or metadynamic recrystallization is expected before quenching, and the fine grains observed experimentally are the dynamically recrystallized grains. This conclusion appears to be consistent with the EBSD and TEM observations showing evidence of substructure within the recrystallized grains.[15] The fraction of dynamic recrystallization increases with increasing strain as expected from the stress-strain curve.

After deformation at a strain rate of 10 s^{-1}, from the ratios of t_{50}* at strains of 0.2 and 0.8 to the quench delay time, the expected statically recrystallized fractions (if the Avrami coefficient is 2) are 5 and 97 pct, respectively, in reasonable agreement with the observed values of 2.3 and 100 pct.[6,15] The physically-based model therefore provides a semiquantitative interpretation of the limited recrystallization data presently available.

Table I. Slip Line Field Corrections

	No Correction			SLF Correction		
Variable	A	α	n	A	α	n
σ_0	1.54×10^{18}	0.0127	10.63	1.54×10^{18}	0.0111	11.68
$\sigma_{0.1}$	1.0×10^{18}	0.0075	7.91	1.0×10^{18}	0.0082	6.61
$\sigma_{ss(e)}$	2.27×10^{18}	0.0065	5.25	2.27×10^{18}	0.0068	4.98
σ_{ss}	0.87×10^{18}	0.0097	3.39	0.87×10^{18}	0.0108	3.43

For both the strain rates studied, the deformation texture evolution with increasing strain was characterized by gradual crystallite rotations toward the stable end texture components located along both the α and β fibers in the Euler space,[8] as expected for PSC deformation of fcc metallic materials largely occurring *via* crystallographic slip.[7,26,27]

Different techniques have been used to model the grain rotations during plastic deformation, and thus to predict deformation texture evolution, each having its limitations and constraints.[28] Recrystallization texture has been modeled separately using different principles.[27] In the present work, a different approach is introduced based on a data-driven systems modeling technique, which uses experimental data for individual orientations with their deformation conditions, and models the rotations of these orientations using neural networks.[23] Such a technique does not depend on the finite element method to produce the deformation conditions, which is time consuming. The data generated (> 3000 points) from the measured textures is used to train the ANN so that the texture evolution can be predicted in a much shorter time. Another advantage of the present modeling technique is that both the deformation and recrystallization texture evolution can be predicted using a common approach.

VII. CONCLUSIONS

A hybrid modeling technique, which uses a combination of empirical, physically-based, and neuro-fuzzy models, has been developed in the present work. The hybrid model has been successfully applied to predict the flow behavior, recrystallization characteristics, and crystallographic texture evolution in a Fe-30 wt pct Ni austenitic model alloy subjected to hot plane strain compression. The flow behavior has been described as a function of the applied variables of strain rate and temperature using an empirical model. The recrystallization characteristics have been predicted from the measured microstructural state variables of internal dislocation density, subgrain size, and misorientation between subgrains using a physically-based model. The evolution of both deformation and recrystallization texture has been modeled using artificial neural networks. The hybrid modeling approach adopted in the present work, which combines physical equations, adaptive numeric modeling, optimization, and metallurgical knowledge, provides a promising tool for modeling industrial hot-working processes in the future.

ACKNOWLEDGMENTS

The authors are grateful to the UK Engineering and Physical Sciences Research Council for financial support through Grant No. GR/L 50198.

REFERENCES

1. S. Almaguer, C.M. Sellars, and W.M. Rainforth: *Proc. 1st Joint Int. Conf. on Recrystallisation and Grain Growth*, G. Gottstein and D.A. Molodov, eds., Springer-Verlag, Aachen, 2001, vol. 2, pp. 831–36.
2. L.J. Swartzendruber, V.P. Itkin, and C. Alcock: *J. Phase Equilibria*, 1991, vol. 12, pp. 288–312.
3. W. Charnock and J. Nutting: *Met. Sci. J.*, 1967, vol. 1, pp. 123–27.
4. M.F. Abbod, J. Talamantes-Silva, Q. Zhu, and D.A. Linkens: *Proc. 2002 IEEE Int. Symp. on Intelligent Control (ISIC2002)*, Vancouver, BC, Canada, Oct. 27–30, 2002, C.W. de Silva and F. Karray, eds., IEEE Control Systems Society, Omnipress, Madison, WI, 2002, pp. 321–26.
5. M.F. Abbod, D.A. Linkens, and Q. Zhu: *Mater. Sci. Eng. A*, 2002, vol. A333, pp. 397–408.
6. F. Bai: Ph.D. Thesis, University of Sheffield, Sheffield, United Kingdom, 2005.
7. V. Randle and O. Engler: *Introduction to Texture Analysis: Macrotexture, Microtexture and Orientation Mapping*, Gordon and Breach Science Publishers, Amsterdam, 2000.
8. H.J. Bunge: *Texture Analysis in Materials Science: Mathematical Methods*, Butterworth and Co, London, 1982.
9. M.S. Loveday, G.J. Mahon, B. Roebuck, A.J. Lacey, E.J. Palmiere, C.M. Sellars, and M.R. van der Winden: *Mater. High Temp.*, 2006, vol. 23, pp. 85–118.
10. R.J. Hand, S.R. Foster, and C.M. Sellars: *Mater. Sci. Technol*, 2000, vol. 16, pp. 442–50.
11. H. Shi, A.J. McLaren, C.M. Sellars, R. Shahani, and R. Bolingbroke: *Mater. Sci. Technol.*, 1997, vol. 13, pp. 210–16.
12. Q. Zhu, H.R. Shercliff, and C.M. Sellars: *Proc. Int. Conf. on Thermomechanical Processing of Steels and Other Materials (THERMEC'97)*, Wollongong, Australia, 1997, T. Chandra and T. Sakai, eds., TMS, Warrendale, PA, 1997, pp. 2039–45.
13. C.M. Sellars and Q. Zhu: *Mater. Sci. Eng.*, 2000, vol. A280, pp. 1–7.
14. F. Bai, P. Cizek, E.J. Palmiere, W.M. Rainforth, and J.H. Beynon: *Mater. Sci. Forum*, 2003, vols. 426–432, pp. 3623–28.
15. F. Bai, P. Cizek, E.J. Palmiere, and W.M. Rainforth: *Mater. Sci. Forum*, 2004, vols. 467–470, pp. 21–26.
16. P. Cizek, J.A. Whiteman, W.M. Rainforth, and J.H. Beynon: *Microsc. J.*, 2004, vol. 213, pp. 285–95.
17. P. Cizek, F. Bai, E.J. Palmiere, and W.M. Rainforth: *J. Microsc.*, 2005, vol. 217, pp. 138–51.
18. F.R. Castro Fernandes, C.M. Sellars, and J.A. Whiteman: *Mater. Sci. Technol.*, 1990, vol. 6, pp. 453–60.
19. Q Zhu, M.F. Abbod, J. Talamantes-Silva, C.M. Sellars, D.A. Linkens, and J.H. Beynon: *Acta Mater.*, 2003, vol. 51, pp. 5051–62.
20. M.F. Abbod, C.M. Sellars, D.A. Linkens, Q. Zhu, and M. Mahfouf: *Mater. Sci. Eng.*, 2005, vol. A395, pp. 901–11.
21. C.M. Sellars and Q. Zhu: *Mater. Sci. Eng.*, 2000, vol. A280, pp. 1–7.
22. C.M. Sellars: *Conf on Hot Working and Forming Processes*, C.M. Sellars, and G.J. Davies, eds., The Metals Society, London, 1980, pp. 3–15.
23. M. Nørgaard: *Neural Networks for Modelling and Control of Dynamic Systems*, Springer, New York, NY, 2000.
24. M.S. Mirza and C.M. Sellars: *Mater. Sci. Technol.*, 2001, vol. 17, pp. 1133–41.
25. B. Kowalski, A.J. Lacey, and C.M. Sellars: *Mater. Sci. Technol.*, 2003, vol. 19, pp. 1564–70.
26. J. Hirsch and K. Lücke: *Acta Metall.*, 1988, vol. 36, p. 2863.
27. F.J. Humphreys and M. Hatherly: *Recrystallisation and Related Annealing Phenomena*, Pergamon, Oxford, United Kingdom, 1996.
28. U.F. Kocks, C.N. Tome, and H.R. Wenk: *Texture and Anisotropy: Preferred Orientations in Polycrystals and Their Effects on Materials Properties*, Cambridge University Press, Cambridge, United Kingdom, 1998.